JOURNAL OF AIRCRAFT
Vol. 42, No. 4, July–August 2005

Effect of Unsteady Blade Pitching Motion on Aerodynamic Performance of Microrotorcraft

Jongmin Kim* and Nikhil Koratkar†
Rensselaer Polytechnic Institute, Troy, New York 12180-3590

The improvement in aerodynamic performance of microscale rotors using unsteady blade motion is investigated using numerical simulations and experimental work. The basic idea is to use dynamic blade pitching motion to delay the onset of stall, enhance the lift, and increase the envelope of operation of small-scale airfoils operating at the low Reynolds number and low Mach numbers that are typical of microrotorcraft. A 22-cm-diam two-bladed microrotor system featuring piezoelectricaly actuated controllable twist rotor blades was developed and tested in hover. The piezoelectric actuation system had sufficient control authority and was able to generate up to ±2.3-deg blade unsteady tip twist deformations under rotating conditions. Excitation of the blade in torsion resulted in significant improvement in the microrotor thrust in the poststall regime. (At 24-deg rotor collective pitch, up to 11% improvement in rotor thrust was demonstrated.) The experimental measurements also showed good agreement with numerical predictions for the effect of dynamic blade pitching on the thrust output and power consumption of the microrotor.

Introduction

ONE of the key aspects of defense planning in the 21st century is the use of swarms of unmanned micro air vehicles (MAVs) that operate in concert with military forces in the battlefield. These unmanned flight vehicles are indispensable for aerial reconnaissance, covert imaging, battlefield management, and for damage assessment. Small-scale vehicles can also be used by civil agencies as information and communication systems, traffic control systems, and biochemical sensors in the field or where regular vehicles do not have the necessary access.

Three basic types of MAV configurations[1] have been explored in the literature: 1) fixed wing, 2) flapping wing, and 3) rotary wing. Fixed-wing designs are unable to hover and perform controlled maneuvers in tightly constraining environments such as interiors of buildings, caves, or tunnels, and this limits their utility for many applications. In contrast to fixed wings, insect-like flapping-wing MAVs take advantage of unsteady aerodynamic phenomenon and are capable of performing highly maneuverable flight at the small scales. However the complex nature of the flowfield, mechanical losses associated with the transmission and control system, and poor stability under adverse atmospheric conditions (such as gusts, turbulence, crosswind, rain, etc.) can prevent the practical implementation of a MAV based upon flapping-wing motion. The third category of MAVs (based on rotary wings) shows promise to provide reliable operation over a wide range of operating conditions, including the hovering and maneuvering capabilities required to remain stationary or in motion in tightly constrained environments. However, because of their scale and flight regime very little is known about the aeromechanics of microscale rotors operating at low Reynolds number and the associated fluid-structure-control interactions at the small scales.

In previous work[2] we have characterized the aerodynamic performance of small-scale rotors in the 10^4 to 3×10^4 tip Reynolds-number range that is typical of rotary-wing MAVs. This involved spin testing of 15-cm-diam microrotors with both baseline NACA 0012 as well as advanced geometry Eppler-61 airfoil sections. The maximum lift-to-drag ratio (L/D) that was generated for the rotor with Eppler-61 airfoil was only about 10 ($C_l \sim 0.96$ and $C_d \sim 0.1$ at $Re = 3.3 \times 10^4$), and the performance of the baseline NACA 0012 airfoil was even 50% lower at the same test conditions (a detailed description of these results is available in Ref. 2). These results are also consistent with recent studies conducted by Bohorquez et al.[3] and Young et al.[4] These performance indices are much lower than full-scale high-performance airfoils that exhibit L/D ratios in the range of 100–150. The reason for this is that in flows below Reynolds numbers of 5×10^4 the viscous effects become dominant,[5,6] leading to severe drag penalties, flow separation at low sectional angles of attack, and a smaller envelope of operation.

Given the poor aerodynamic efficiency ($L/D < 10$), low figure of merit (ratio of induced to total power < 0.5) of microscale rotors,[2–4] and the limitations of current battery technology,[7] it is not possible to meet the flight envelope for MAVs because of the extreme power requirements. With present efficiency levels the maximum endurance demonstrated by battery powered MAVs has been ~20 min [only 35% of Defense Advanced Research Projects Agency goal of 60 min fully autonomous flight]. Therefore it is critical to develop new strategies to improve the aerodynamic efficiency of microscale rotors to enable efficient, sustained, and controllable flight at the microscale. One such approach might be to exploit dynamic (or delayed) stall to achieve substantial improvements in MAV aerodynamic performance.

Approach

Dynamic stall will occur when the airfoil is subjected to time-dependent pitching, plunging, or vertical translation, or other type of nonsteady motion that takes the effective angle of attack above its normal static-stall value. Under these circumstances, the physics of flow separation and the development of stall have been shown to be fundamentally different[8–11] from the stall mechanism exhibited by the same airfoil under static conditions. Dynamic stall is distinguished by a delay in the onset of flow separation to a higher angle of attack compared to the static case. This initial delay in stall onset is advantageous as far as the performance and operational flight envelope of the airfoil is concerned.

It has been shown that the delayed-stall mechanism[8–10] is related to shedding of a concentrated vortical disturbance from the leading-edge region of the airfoil that is subsequently swept over the airfoil chord. Such a shed vorticity serves to energize the boundary layer for full-scale airfoils enabling it to remain attached at higher angles of attack. This paper will investigate whether a similar performance

Received 26 November 2003; revision received 7 October 2004; accepted for publication 12 October 2004.

*Graduate Research Assistant, Department of Mechanical, Aerospace, and Nuclear Engineering. Student Member AIAA.
†Assistant Professor, Department of Mechanical, Aerospace, and Nuclear Engineering. Member AIAA.

benefit (improved maximum lifting capability caused by delayed flow separation) can be realized for the small-scale airfoils used on microrotor blades.

In this study a compact, lightweight, low-power piezoelectric actuation system is used to induce dynamic blade-pitch oscillations. (The amplitude and frequency of the blade deformations are controlled via the control signal to the piezoelectric actuators.) A finite element structural model is developed to predict the blade torsion deformations caused by the piezoinduced-strain actuation and validated using nonrotating testing on the bench top. The structural model is also coupled to a blade-element aerodynamic model[12] with linear inflow to predict the blade-twist deformations under rotating conditions. The results indicate the piezoelectric actuation system has sufficient control authority to actively twist the microblades under rotating conditions.

Next, the microrotor system with active control of blade twist is tested in hover using a small-scale rotor test rig (instrumented with a slip ring unit to enable on-blade actuation in the rotating frame). Tests are conducted at several different excitation frequencies and blade collective pitch settings, and the resulting changes to the microrotor's thrust output and power consumption are recorded. The results indicate that delayed stall at the microscales can result in significant improvement in rotor performance in the post-stall regime. The measured rotor airloads are also compared with unsteady Navier–Stokes flow simulations (conducted using Fluent), and good agreement between the computational fluid dynamics simulations and test data is achieved for both the rotor thrust output and power consumption. A detailed description of these studies is described in the following sections.

Microblade Fabrication

Piezoelectric materials strain when an electric field is applied across them. This property makes them suitable as actuators to control blade structural response. The actuation system for microblade twisting and bending consists of high-aspect-ratio piezoelectric elements oriented at ±45 deg to the blade axis (Fig. 1). The feasibility of this actuation mechanism has been demonstrated in previous studies by several researchers.[13–15] Simultaneous in phase-induced-strain actuation of the piezoelements on the top and bottom surfaces results in a net shear strain causing the blade to twist. In the same way an out-of-phase actuation on the top and bottom surfaces causes flat-wise bending of the rotor blades. The amplitude, phase, and frequency of blade twisting and bending can be accurately controlled using the voltage input to the piezoelectric actuators.

There are several important issues concerning blade fabrication. These include the following 1) electric contact on both sides of piezosheet is required; 2) piezopatch has to be insulated from the blade; and 3) for proper transfer of induced strain to blade, bond layer thickness needs to be thin and uniform. For the present microrotor system, the piezoelectric elements are surface bonded at +45 deg with respect to the blade axis on the top surface and at −45 deg on the bottom surface. The choice of piezoelectric actuators is governed by their low power consumption and high operating bandwidth. Torsionally soft polymer blades (shown in Fig. 1) are used in this study. The piezoelements are surface bonded close to the hub near the blade-root region to minimize the disruption of the flowfield.

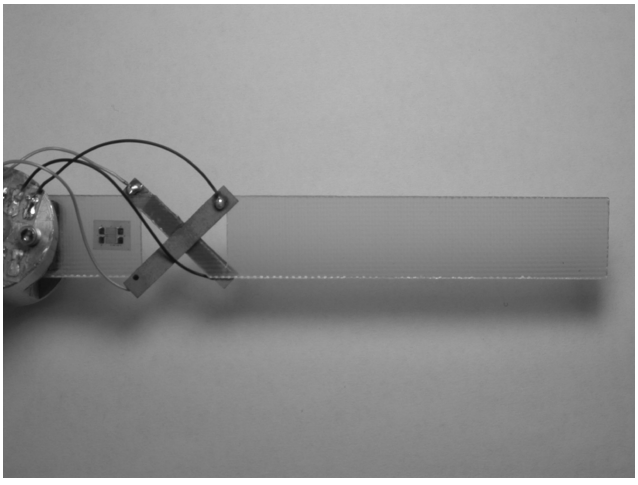

Fig. 1 Microrotor blades with surface-mounted piezoceramic actuation elements oriented at ±45 deg to the blade axis. The blades are manufactured using a torsionaly soft polymer material to maximize the twist response.

Dynamic Model for Piezoactuated Blade-Twist Response

The microrotor blade shown in Fig. 1 is modeled as an elastic beam undergoing flap bending and elastic twist. Although deflections are considered to be moderately large, strains are assumed to be small. The analysis takes into account precone and chordwise offsets of the blade center of gravity and aerodynamic center from the elastic axis. Furthermore the blades are modeled as isotropic Bernoulli–Euler beams; therefore, nonlinear strain-displacement relations can be based on the deformed configuration directly.

A piezoelectric patch of length l_c, width b_c, and thickness t_c is attached to the blade surface. If an electric field (voltage V) is applied, then the force transfer to the blade can be expressed as

$$F_p = d_{31} E_c b_c V \sin\beta \tag{1}$$

where E_c is Young modulus of elasticity of piezosheet, d_{31} is the piezoelectric constant, and β is the offset angle from the blade axis.

The torsion moment transferred to the blade axis is given by

$$M_p = d_{31} E_c b_c V \sin\beta\, d \tag{2}$$

where d is the vertical separation between the actuators on the top and bottom surfaces.

Hamilton's variational principle is used to derive the system equations of motion, which can be written as

$$\int_{t_1}^{t_2} (\delta U - \delta T - \delta W)\, \mathrm{d}t = 0 \tag{3}$$

where δU is the virtual variation of strain energy, δT is virtual variation of kinetic energy, and δW is the virtual work done by external forces.

Variation of strain energy is determined using the uniaxial stress assumption and corresponding stress–strain relationships and is expressed as follows:

$$\delta U = \int_0^R \iint_A (E\varepsilon_{xx}\delta\varepsilon_{xx} + G\varepsilon_{x\eta}\delta\varepsilon_{x\eta} + G\varepsilon_{x\zeta}\delta\varepsilon_{x\zeta})\, \mathrm{d}\eta\, \mathrm{d}\zeta\, \mathrm{d}x \tag{4}$$

where ε_{xx} is the axial strain and $\varepsilon_{x\eta}$ and $\varepsilon_{x\zeta}$ are engineering shear strains. The expressions for the strain components are available in Ref. 16.

The kinetic energy of the blade depends on blade in-plane and out-of-plane bending and torsion deflection relative to the hub-fixed frame of reference. The position vector $\boldsymbol{r}$ of an arbitrary point on the blade is differentiated with respect to the hub-fixed nonrotating system to obtain the velocity vector $\boldsymbol{V}$. The variation of kinetic energy is calculated using

$$\delta T = \int_0^R \iint_A \rho_s \boldsymbol{V} \cdot \delta \boldsymbol{V}\, \mathrm{d}\eta\, \mathrm{d}\zeta\, \mathrm{d}x \tag{5}$$

where $\boldsymbol{V}$ is the blade velocity and ρ_s is the mass density of the blade.

Both external aerodynamic forces acting on the rotor blades and the actuation moments induced by the piezoelements [Eqs. (1) and (2)] will contribute to the virtual work of the system. The aerodynamic formulation[16] is based on quasi-steady aerodynamics and linear inflow modeling. The radial, tangential, and induced velocities are derived in the rotating frame of reference, and two-dimensional

strip theory is used to determine the rotor-blade virtual work for the ith element, which is expressed as

$$[\delta W_A]_i = \delta \boldsymbol{q}_i^T (M_A \ddot{\boldsymbol{q}} + C_A \dot{\boldsymbol{q}} + K_A \boldsymbol{q} + \boldsymbol{Q}_A)_i \tag{6}$$

where M_A, C_A, and K_A are the mass, damping, and stiffness matrices caused by aerodynamic effect respectively; $\boldsymbol{Q}_A$ is the load vector; and $\boldsymbol{q}$ is the blade nodal displacement vector.

The virtual energy expression for the blade is written in the discretized form as follows:

$$\sum_{i=1}^{N} (\delta U_i - \delta T_i - \delta W_i) = 0 \tag{7}$$

where i is the ith beam element and N is the total number of spatial finite elements in the blade. A finite element with seven degrees of freedom is used for the present study. These degrees of freedom correspond to cubic variations in elastic flap bending deflections and quadratic variation in elastic twist. Spatial discretization of Hamilton's principle results in the rotor-blade equation of motion after imposing the hingeless displacement boundary conditions:

$$M\ddot{q} + C\dot{q} + Kq = \boldsymbol{Q} \tag{8}$$

where M, C, and K are the assembled global mass, damping, and stiffness matrices, respectively, for the microblade, and $\boldsymbol{Q}$ is the global load vector related to the piezoelectric and aerodynamic forces.

Nonrotating-Blade Twist Characterization

For the nonrotating-blade response, only structural mass M_s and stiffness K_s from Eqs. (4) and (5) and torsional moment M_p caused by piezoelectric force from Eq. (2) are considered. In this case the rotor-blade equation of motion is as follows:

$$M_S\ddot{q} + K_S q = M_P \exp(i\omega t) \tag{9}$$

The transfer receptance $\alpha_{jk}(\omega)$, which represent the response in degree of freedom j caused by harmonic force of unit magnitude and frequency ω applied in degree of freedom k, can be obtained as

$$\alpha_{jk}(\omega) = \sum_{r=1}^{n} \frac{\phi_{jr}\phi_{\mathrm{kr}}}{\left(\omega_r^2 - \omega^2\right)} \tag{10}$$

where Φ are the eigenvectors of the system. Figure 2 shows the nonrotating tip twist response for the polymer blade obtained using Eq. 10 (with 200 Vrms/mm electric field applied to the piezoceramic actuators). Experimental bench-top (nonrotating) test data are also plotted for comparison; the predictions of the numerical model show good agreement with measurements. The results indicate that the piezoelectric actuation system can generate significant blade-tip twist amplitudes in the 0–300 Hz frequency range. The nonrotating torsional natural frequency of the microblades is estimated as 210 Hz (Fig. 2). At this frequency over ±14 deg of blade-tip twist angles are achieved for a 200 Vrms/mm excitation to the piezoelements on the top and bottom blade surfaces.

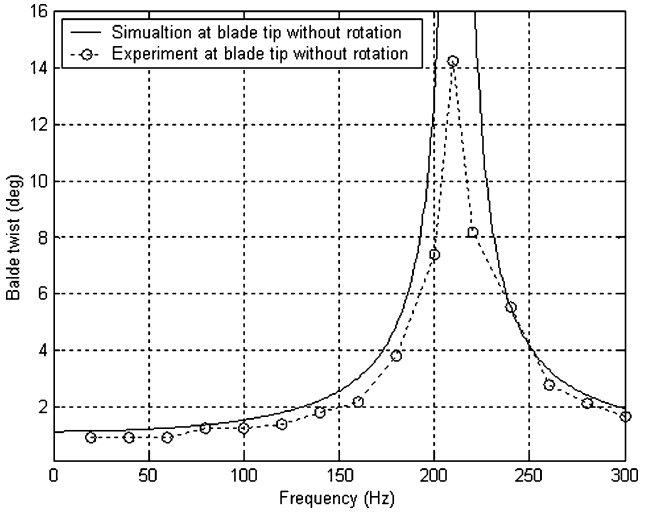

Fig. 2 Nonrotating twist response of piezoelectrically actuated microrotor blades. (Electric field input to piezoactuators is 200 Vrms/mm.)

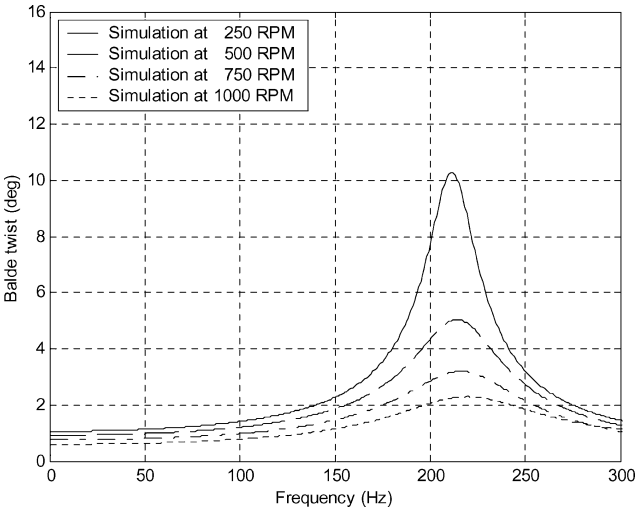

Fig. 3 Predicted blade-tip twist response (200 Vrms/mm input to piezoactuators) at different rotor speeds (250–1000 rpm) at 24-deg rotor collective pitch setting.

Predicted Blade-Twist Response Under Rotation

To study the actuator response under rotating conditions, simulations were conducted in the 0–1000 rpm range. The blade-tip Mach number and Reynolds number (at 1000 rpm rotor speed) are 0.0339 and 12×10^3, respectively. For the rotating-blade response, we conducted the modal analysis using Eq. (8). Figure 3 shows the predicted blade-tip twist response as a function of piezoelectric activation frequency for different rotor speeds. The collective pitch setting is 24 deg, and the excitation amplitude is 200 Vrms/mm to the piezoactuators. The tip twist amplitude in the low-frequency range (0–100 Hz) at 1000 rpm is about 0.5 deg compared to ~0.9 deg under nonrotating conditions. The natural frequency has shifted from ~210 Hz (at 0 rpm) to about 220 Hz (at 1000 rpm) as a result of aerodynamic stiffening, and the blade-tip twist amplitude is about 2.3 deg at the torsional natural frequency, which is significantly lower than under nonrotating conditions. This can be attributed to the aerodynamic damping of the blade torsion mode. Note that although the Lock number of the microrotor (~2.0) is small in comparison to large-scale rotors, the relatively large chordwise offset between aerodynamic center and elastic axis and high sectional drag coefficient associated with the low-Reynolds-number flow results in significant torsion mode damping under rotating conditions. Figure 4 shows the effect of rotor collective pitch on the dynamic blade-tip twist response at 1000 rpm in the 0–300 Hz frequency range (200 Vrms/mm input to the piezoactuators). Although a slight reduction in the torsional natural frequency and torsion mode damping is seen with increasing collective, the blade-tip twist amplitudes are not significantly affected by collective pitch settings.

Effect on Blade Dynamic Pitching on Microrotor Airloads

The simulations (shown in Figs. 3 and 4) predict that up to ±2.3-deg blade unsteady tip twist deformations can be generated by the actuation system under rotating conditions. To study the effect of dynamic blade pitching on the microrotor's aerodynamic performance, whirl tests were performed using a small-scale rotor test rig. Actuator amplitude and frequency sweep tests were conducted at 1000 rpm for different blade collective pitch settings, and the rotor

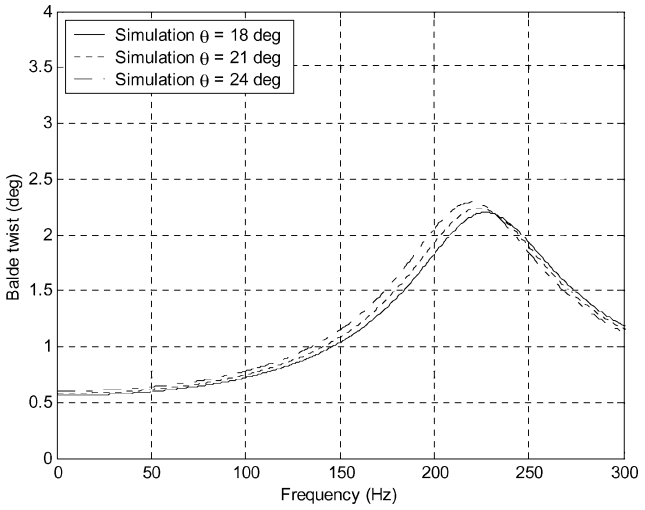

Fig. 4 Predicted blade-tip twist response (200 Vrms/mm input to piezoactuators) for different collective pitch settings at a rotor speed of 1000 rpm.

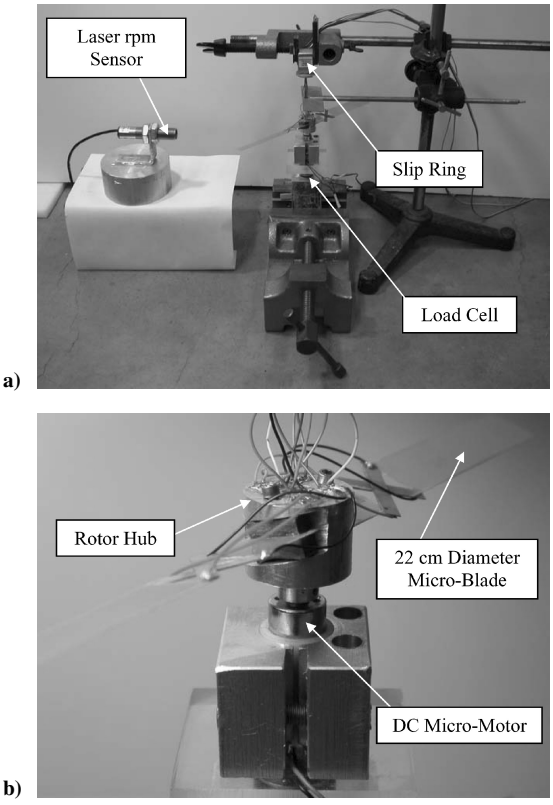

Fig. 5 Test rig and whirl tower for small-scale rotor experiments: a) load cell, rotor speed sensor and slip ring unit; b) micro-rotor-blade assembly and hub fixtures.

thrust and power consumption were carefully monitored to study the delayed stall effects at the microscale. First we describe the microrotor test rig used to perform the experiments followed by the test results and comparison with CFD results.

Microrotor Test Platform

The experimental set up consists of a highly sensitive load cell (least count of 0.02 g) for measuring rotor thrust, a laser light source coupled to a frequency counter to measure rotor speed, and a microcoreless dc motor with associated fixtures that connect the microblades to the motor output spindle. The motor is driven by means of a dc power supply. Figure 5a shows the microrotor test platform instrumented with a slip ring to enable electrical activation of rotor blades in the rotating frame. The diameter of the microrotor used for the present test is 22 cm. A clearance of 25 cm (more than twice the micro-rotor radius) is maintained to minimize ground effect.[17] Figure 5b shows a close-up view of the microrotor blades, micro-dc motor, and hub attachment fixtures. The blades can be connected to the hub at adjustable collective pitch settings ranging from 0–24 deg; all tests are performed in the two-bladed rotor mode. The microrotor blades are tested at 1000 rpm (tip Mach number of 0.0339 and tip Reynolds number of 1.2×10^4). The blade planform is rectangular (no taper, sweep, or twist), aspect ratio is 7.33 (11-cm radius and 1.5-cm cord), and airfoil section is NACA 0012. The blade-root cutout is approximately 35% of the rotor radius.

Rotor Thrust Measurements and Comparison with Computational-Fluid-Dynamics Predictions

Figure 6 plots the percentage improvement in rotor thrust as a function of blade excitation frequency at different collective pitch settings. The results indicate that the rotor lifting capacity is enhanced by ~11.5% at a rotor collective pitch of 24 deg. However this improvement is seen only at the blade torsion natural frequency (~220 Hz). This is because of relatively large blade unsteady pitching motion (±2.3 deg, Figs. 3 and 4) that occurs at the torsion mode. This pitching motion delays the onset of flow separation as a result of the boundary layer being energized by harmonic shed vorticity resulting from the blade-pitch oscillations. At actuation frequencies other than 220 Hz, the blade torsional response appears to be too low to significantly influence the airfoil stall characteristics.

Figure 6 also shows the effect of collective pitch on the improvement in rotor lift. Below a collective pitch setting of 18 deg, no significant improvement in performance was seen. For 21-deg collective pitch, the improvement is about 7%, and at 24 deg it is 11%. This suggests that below 18-deg pitch the rotor lies in the prestall regime, and so unsteady blade motion does not affect the response. As the rotor blade transitions into stall at 18-deg pitch, the performance is enhanced by the piezoelectric actuation. Finally when the rotor is completely stalled at 24 deg, the maximum benefit of the pitch oscillations in delaying the onset of stall can be obtained.

It is important to differentiate between the collective pitch and the angle of attack. The pitch setting is a constant for the entire blade, whereas the angle of attack varies along the blade span and is obtained by subtracting the local inflow angle from the collective pitch setting. For the 75% span airfoil that is representative of the rotor, the effective angle-of-attack variation with collective pitch is shown in Fig. 7a using blade-element momentum theory in hover.[11,12] From the figure we see that collective pitch settings of 18, 21, and 24 deg correspond to angle-of-attack settings of approximately 11, 14, and 17 deg, respectively. To confirm that the airfoil transitions into stall

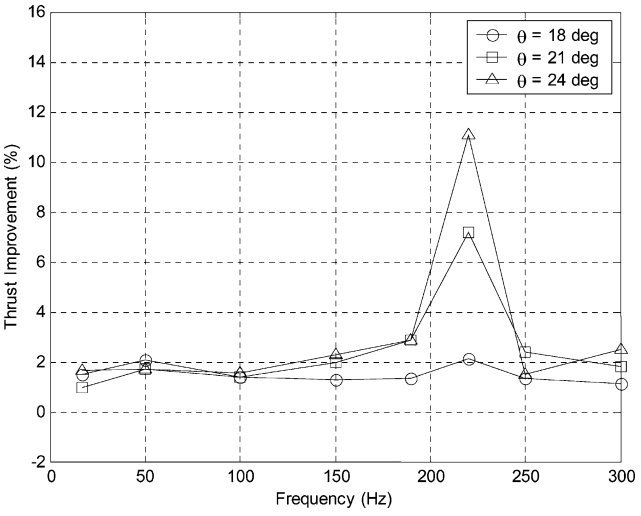

Fig. 6 Percentage change in steady rotor thrust vs excitation frequency (input to piezoactuators is 200 Vrms/mm) at three different rotor collective pitch settings.

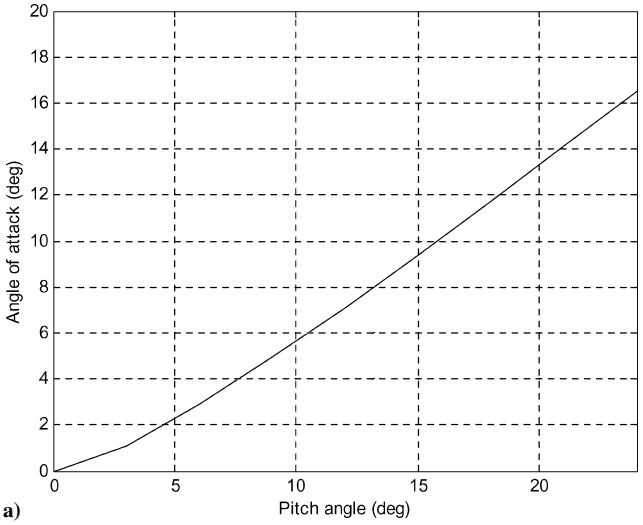

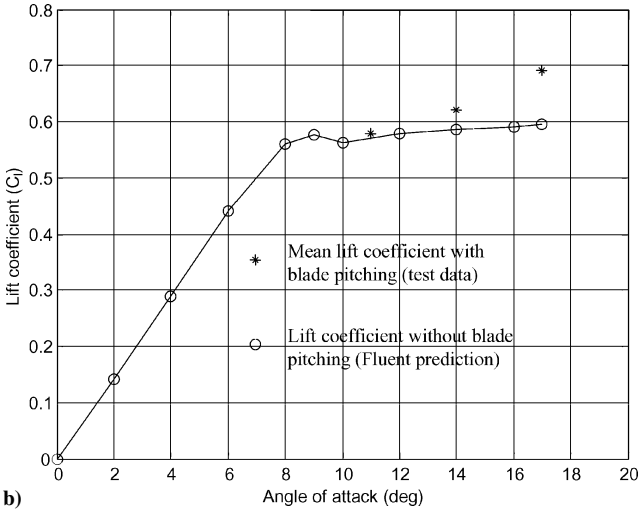

Fig. 7 Performance and stall characteristics of baseline microblade airfoil section located at 75% of blade span (Mach number of 0.0254 and Reynolds number of 9×10^3): a) angle of attack at 75% blade spanwise location for different rotor collective pitch settings; b) airfoil mean lift coefficient at 75% blade spanwise location.

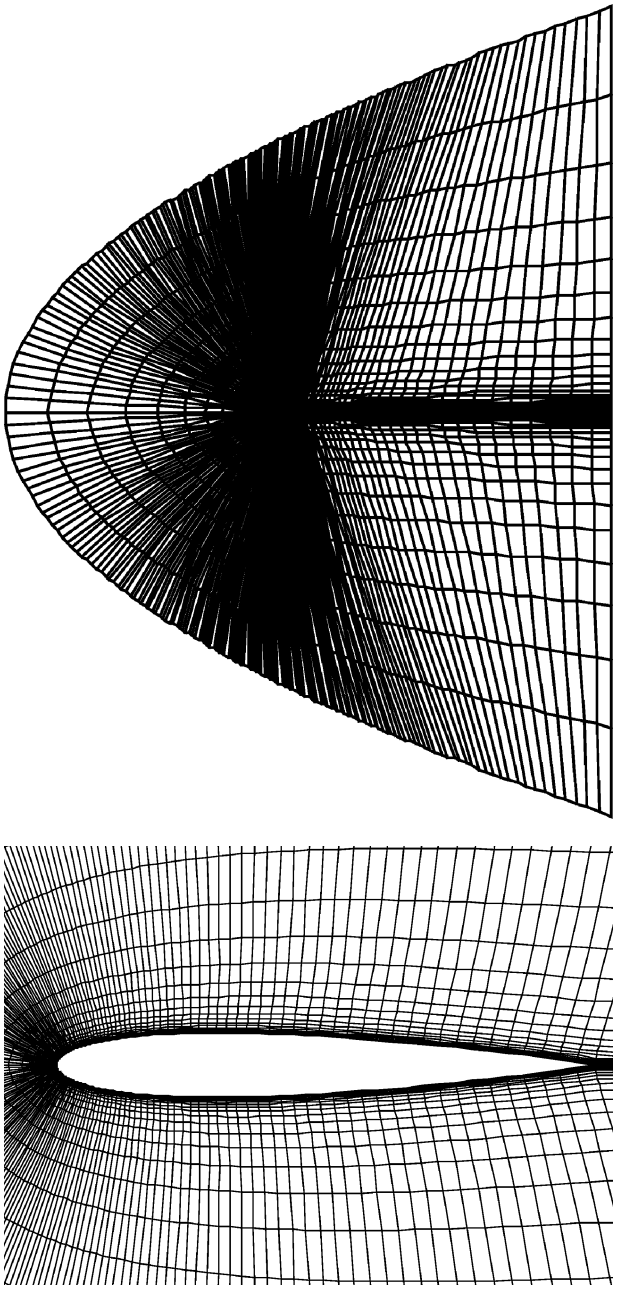

Fig. 8 Control volume and computational mesh around the airfoil for CFD simulations.

close to a collective pitch setting of 18 deg (i.e., at an airfoil angle of attack of about 11 deg), we performed numerical flow simulations using the commercially available Navier–Stokes flow solver Fluent. Figure 7b shows the results of the simulations for the airfoil section at 75% spanwise location (chord Reynolds number 9×10^3 and Mach number 0.0254). Figure 7b shows that the predicted-stall onset angle lies in the 9–10 deg range, indicating that the microrotor will in all likelihood be stalled beyond about 16–18 deg collective pitch. Test data from Fig. 6 for the active rotor thrust were used to estimate (using blade-element theory) the airfoil sectional lift coefficient at 75% span and are also shown in Fig. 7b for comparison. The results confirm that the full impact of unsteady blade pitching in enhancing lift and improving the airfoil performance is seen only in the deep-stall regime.

Simulations using Fluent for the solution of the unsteady Navier–Stokes equations for a microscale airfoil were also conducted and compared with the measured test data. The dynamic mesh model in Fluent is used to model flow where the shape of the domain is changing with time as a result of oscillation (dynamic pitching) of the airfoil section. The airfoil motion is specified by the angular velocity about the elastic axis of the airfoil using user-defined function in Fluent. The airfoil upper and lower surfaces are described by polynomial interpolation functions to the given airfoil geometry. The far-field (outer) control surface is described by a parabolic surface of about 20 airfoil chords away from the airfoil leading edge that is cut by a vertical segment far downstream of the airfoil (Fig. 8). A structured computational grid composed of quadrilateral cells is constructed in the flow control volume between the airfoil and far-field surfaces with K radial grid lines and L circumferential grid lines (a mesh of $K \times L$). The cells are clustered near the airfoil such that the cells nearest to the surface have high aspect ratios to accurately capture the flow in the very thin velocity boundary layers. Perfect-gas law is used for the equation of state, specific heat is held constant, and Sutherland law is used to take into account effect of temperature on viscosity and thermal conductivity. The far-field conditions model a freestream uniform flow with prescribed freestream Mach number, static pressure, and temperature, whereas along the airfoil surfaces the no-penetration and no-slip boundary conditions are imposed. An implicit and iterative, second-order procedure is used to integrate the continuity, momentum, and energy equations and calculate the unsteady-state fields of velocity, temperature, density, and pressure.

Numerical simulations were conducted with varying levels of mesh refinement. For this study, the gradients normal to the airfoil

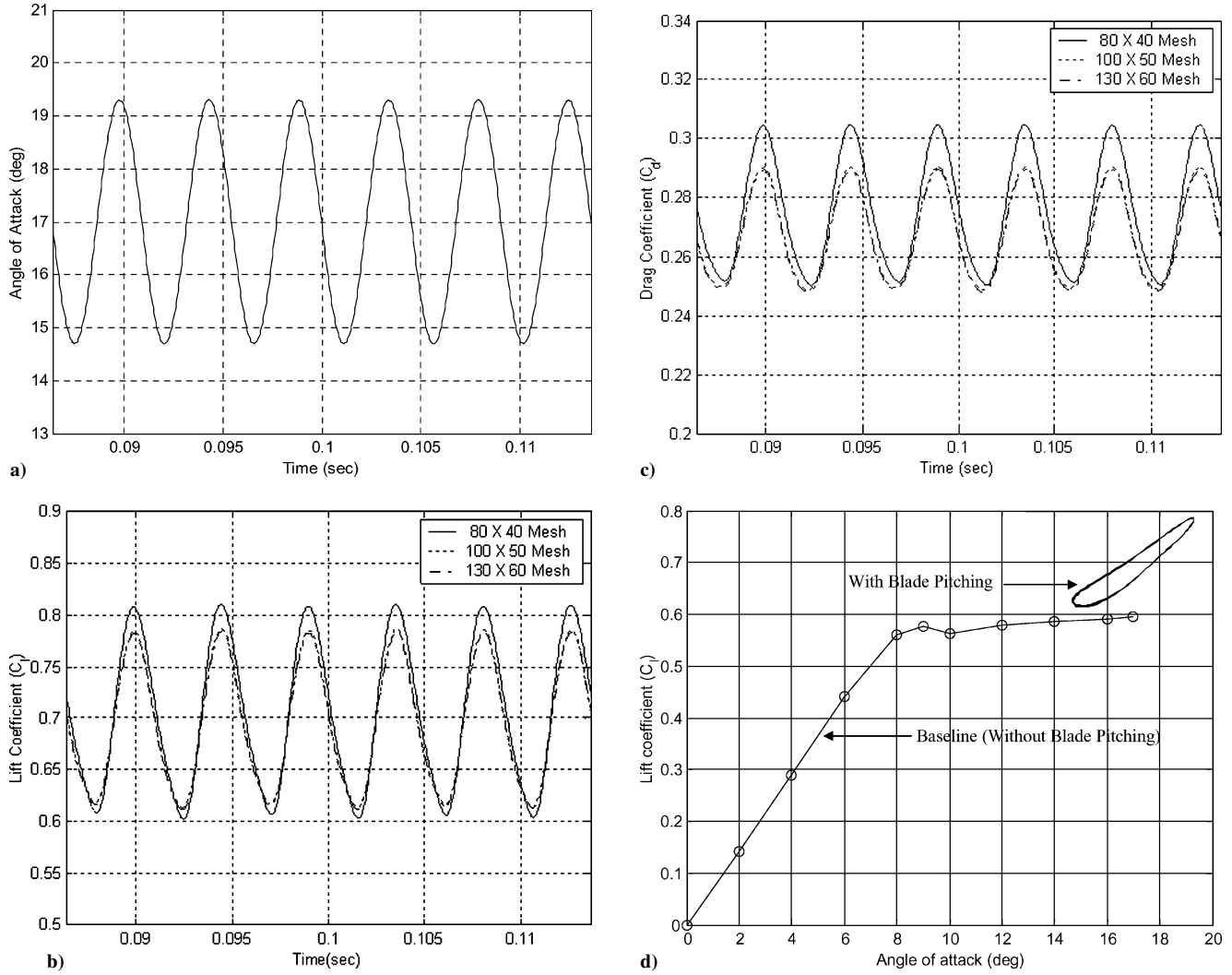

Fig. 9 Numerical verification studies performed for a uniform flow of air with Mach number of 0.0254 and Reynolds number of 9×10^3 around a NACA 0012 airfoil under prescribed unsteady airfoil pitching motion with amplitude of ± 2.3 deg and frequency of 220 Hz: a) prescribed unsteady airfoil motion (± 2.3 deg at 220 Hz) at 17-deg mean angle of attack, b) lift coefficient vs time for various meshes at 17-deg mean angle of attack, c) drag coefficient vs time for various meshes at 17-deg mean angle of attack, and d) lift vs angle of attack polar for the 50×100 mesh; static case is also shown for comparison.

surface are much greater than those tangential to the airfoil, except near the leading and trailing edges. Consequently, the quadrilateral cells nearest the surface have very high aspect ratios. Mesh convergence studies were performed for the case of a uniform flow of air around a NACA 0012 airfoil with Mach number 0.0254, Reynolds number 9×10^3 (corresponding to a representative airfoil at 75% microblade span spinning at 1000 rpm), and freestream pressure and temperature of 1 atm and 300 K, respectively. The time history of angle-of-attack variation is shown in Fig. 9a. Unsteady motion of airfoil is prescribed by amplitude of ± 2.3 deg and frequency of 220 Hz at 17-deg mean angle of attack. Results of the computations with various meshes are shown in Figs. 9b and 9c. Figures 9b and 9c show the lift and drag coefficient as a function of time, respectively with a mesh of 80×40 (7200 cells), 100×50 (9800 cells), and 130×60 (19,000 cells). The results with a mesh of 80×40 show an overprediction of the lift and drag coefficient near the peak region leading to a corresponding overprediction of mean lift and drag coefficient. However, for finer mesh of 100×50 and beyond, no significant change in the solution is observed. Note that the drag coefficient is very high because the flow is in deep-stall regime. We conclude from Figs. 9b and 9c that a mesh of 100×50 is sufficient for a converged (mesh-independent) flow solution, and this mesh is used in all of the following computations. Figure 9d shows the Fluent prediction for the lift vs angle-of-attack polar for the angle-of-attack perturbation shown in Fig. 9a. The baseline steady result (no actuation case) is also shown for comparison. The predictions for the dynamic (active) rotor response show clear deviations from the static curve in the poststall regime; this is consistent with the test results shown in Fig. 7b.

To compute the rotor thrust, the predicted dynamic airfoil pitching amplitude obtained from Eq. (8) (for each excitation frequency and collective pitch setting) is applied to a number of discrete blade elements along the rotor span. The computational-fluid-dynamics (CFD) flow solver just described is used to generate the unsteady airfoil lift at each section along the span, which is then averaged to obtain the mean lift coefficient. This mean airfoil lift coefficient for each individual blade element is used in conjunction with blade-element momentum theory[11] to predict the total integrated thrust output of the microrotor. Figure 10 compares the experimental data with the numerical simulations for the 24-deg collective pitch case. The predictions of the numerical simulations show good correlation with the measurements. For example, the estimated thrust increase is 3.7% with an exciting frequency of 190 Hz and 11.8% with 220 Hz. The experimental results show 2.9 and 11.5% for each case.

Rotor Power Measurements and Comparison with CFD Predictions

Note that although the lift is enhanced by the dynamic- or delayed-stall effects, the airfoil drag can also be increased as a result of the continuous shedding of vorticity from the leading edge. To compute rotor power, the unsteady airfoil drag computed using CFD was time averaged, and the mean drag coefficient for each blade element

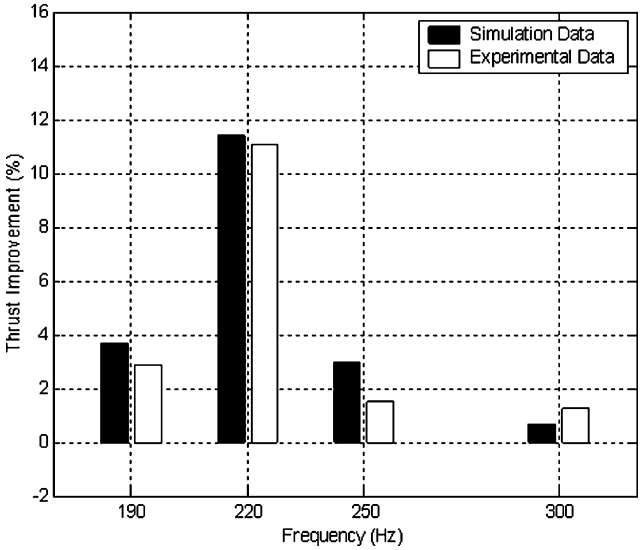

Fig. 10 Comparison of predictions and test data for mean rotor thrust at 24-deg collective pitch setting for a 200 Vrms/mm electric field input to the piezoelectric actuators.

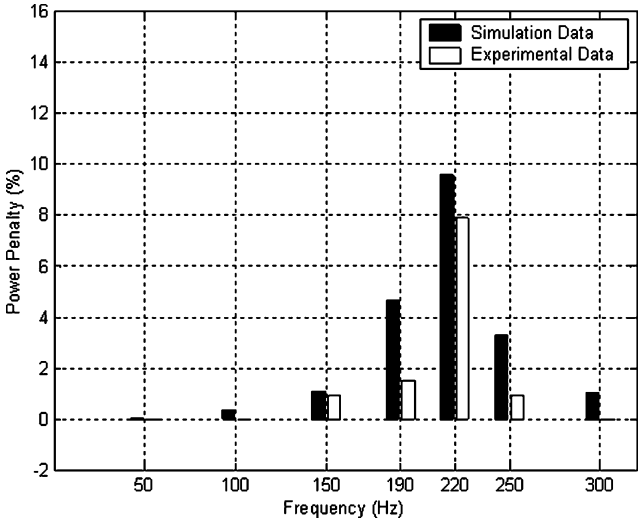

Fig. 11 Comparison of predictions and test data for mean rotor power at 24-deg collective pitch setting for a 200 Vrms/mm electric field input to the piezoelectric actuators.

along the span was used to calculate the rotor power consumption. Figure 11 shows the increase in rotor power for the 24-deg collective pitch case over a range of excitation frequencies using both experimental and numerical simulation. The increase in rotor power was experimentally estimated by monitoring the excess power supplied to the dc motor in order to maintain a constant rotor speed (1000 rpm) with the blade actuation turned ON. Both test data and numerical predictions show similar trends (power consumed increases caused by blade-pitch oscillations) with the numerical model overpredicting the power penalty. For example, the estimated power penalty is 1.1% at a blade-pitch exciting frequency of 150 Hz and 9.6% at 220 Hz. The experimental results show 0.9 and 7.2% for each case. Although the rotor aerodynamic power consumption increases as a result of blade pitching, the overall thrust-to-power ratio (in the 20–24-deg collective pitch range) shows ∼5% increase compared to the baseline condition with the actuation turned OFF.

In addition to the dc power supplied by the battery to drive the micromotor, ac power must also be supplied to the microblades for actuating the piezoelectric sheets. Figure 12 shows the piezoelectric power consumption at different frequencies. The power consumed by the actuation system at 220 Hz is about 1.08 W. The dc power supplied by the motor for operation at 24-deg collective at 1000 rpm is also shown in Fig. 12 for comparison. In this study the actuator

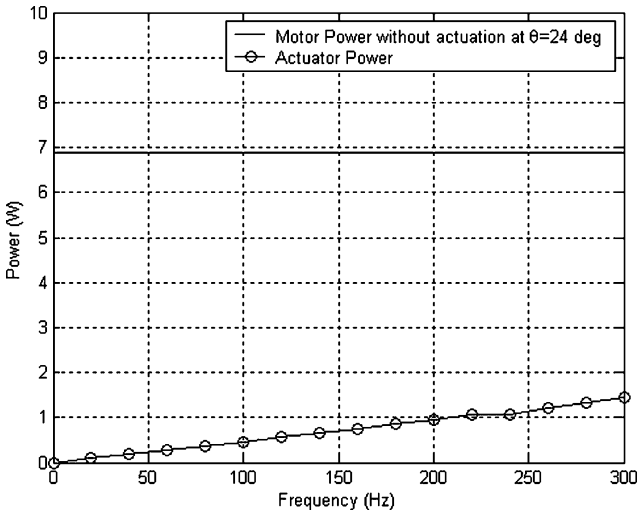

Fig. 12 Power consumption of the actuation system at several different excitation frequencies for a 200 Vrms/mm input to the piezoelectric sheets.

and blade design was not optimized, and we believe that the actuator power requirements can be significantly decreased by tailoring blade structural properties, by the use of mechanical torsion hinges and by use of improved actuator materials such as piezoelectric fiber composites.

Summary

The improvement of aerodynamic performance of microscale rotors using unsteady blade pitching motion was investigated using numerical simulations and experimental work. The objective was use dynamic blade pitching motion to delay the onset of stall, enhance the lift, and increase the envelope of operation of small-scale airfoils operating at the low Reynolds number and low Mach numbers that are typical of microrotorcraft. Blade actuation was achieved using the induced-strain response of piezoelectric patches bonded close to the blade root at ±45 deg with respect to the blade axis. The piezoelectric actuators were chosen because of their compact, lightweight design and low power consumption.

Spin tests were conducted using a 22-cm-diam microrotor system featuring piezoelectricaly actuated controllable twist rotor blades. The piezoelectric actuation system had sufficient control authority and was able to generate up to ±2.3-deg blade unsteady tip twist deformations under rotating conditions. The study indicated that unsteady blade pitching motion has a significant impact on the lifting capability of the microrotor in the poststall regime. An 11% increase in lift is achieved at 24-deg collective pitch, with 220-Hz activation of the piezoelectric materials. Although the rotor power also increased by ∼7% as a result of the shed vorticity, the overall microrotor thrust-to-power ratio was enhanced by about 5% in the 20–24-deg collective pitch range. The experimental measurements also showed good agreement with finite element model predictions for the piezo-induced blade-twist response and computational fluid dynamics predictions for the effect of unsteady blade pitching motion on the microrotor thrust and power.

These results indicate that unsteady blade motion shows potential to enhance lift, improve efficiency (thrust-to-power ratio), and expand the envelope of operation of microscale rotors. Future work will focus on extensive parametric studies using the numerical model to study the conditions under which the microrotor thrust can be maximized with minimal power penalty. Optimization of the microrotor blade's mass and stiffness distribution and new improved actuator materials (such as embedded piezoelectric fibers) will also be investigated to maximize the overall system performance.

References

[1]Ellington, C. P., and Usherwood, J. R., "Lift and Drag Characteristics of Rotary and Flapping Wings," *Fixed and Flapping Wing Aerodynamics for Micro Air Vehicle Applications*, edited by T. J. Mueller, Progress in

Aeronautics and Astronautics, Vol. 195, AIAA, Reston, VA, 2001, Chap. 12, pp. 231–248.

[2]Gray, N., Kim, J., and Koratkar, N., "Aerodynamic Design Considerations for Micro-Rotorcraft," *Proceedings of the AHS 58th Annual Forum and Technology Display*, edited by D. Newman, Vol. 2, American Helicopter Society, Alexandria, VA, 2002, pp. 2181–2197.

[3]Bohorquez, P., Samuel, P., Sirohi, J., Pines, D., Rudd, L., and Perel, R., "Design, Analysis and Hover Performance of a Rotary-Wing Micro-Air-Vehicle," *AHS Journal*, Vol. 48, No. 2, 2003, pp. 80–90.

[4]Young, L., Aiken, E., Johnson, J., Demblewski, R., Andrews, J., and Klem, J., "New Concepts and Perspectives on Micro-Rotorcraft and Small Autonomous Rotary-Wing Vehicles," *Proceedings of the 20th AIAA Applied Aerodynamics Conference*, AIAA, Reston, VA, 2002.

[5]Mueller, T. J., and Jansen, B. J., "Aerodynamic Measurements at Low Reynolds Numbers," AIAA Paper 82-0598, March 1982.

[6]O'Meara, M. M., and Mueller, T. J., "Laminar Separation Bubble Characteristics on an Airfoil at Low Reynolds Numbers," *AIAA Journal*, Vol. 25, No. 8, 1987, pp. 1033–1041.

[7]Zbikowski, R., Pedersen, C., Hameed, A., Friend, C., and Barton, P., "Current Research on Flapping Wing Micro Air Vehicles at Srivenham," AVT Symposium on Unmanned Vehicles for Aerial, Ground and Naval Military Operations, Oct. 2000.

[8]Beddoes, T. S., "Onset of Leading-Edge Separation Effects Under Dynamic Conditions and Low Mach Number," *34th Annual Forum of the American Helicopter Society*, May 1978.

[9]Leishman, J. G., and Beddoes, T. S., "A Semi-Empirical Model for Dynamic Stall," *Journal of the American Helicopter Society*, Vol. 34, No. 3, 1989, pp. 3–17.

[10]Leishman, J. G., "Modeling Sweep Effects on Dynamic Stall," *Journal of the American Helicopter Society*, Vol. 34, No. 3, 1989, pp. 18–29.

[11]Leishman, J. G., *Principles of Helicopter Aerodynamics*, Cambridge Univ. Press, Cambridge, England, U.K., 2000, Chap. 9, pp. 378–414.

[12]Koratkar, N., and Chopra, I., "Analysis and Testing of a Mach-Scaled Rotor Model with Trailing-Edge Flaps," *AIAA Journal*, Vol. 38, No. 7, 2000, pp. 1113–1124.

[13]Chen, P., and Chopra, I., "Development of a Smart Rotor Blade with Induced Strain Actuation of Blade Twist," *AIAA Journal*, Vol. 35, No. 1, 1997, pp. 6–11.

[14]Bent, A., and Hagood, N. W., "Piezoelectric Fiber Composites with Interdigitated Electrodes," *Journal of Intelligent Materials Systems and Structures*, Vol. 8, No. 11, 1997, pp. 903–919.

[15]Wilbur, M. L., Mirick, P. H., Yeager, W. T., Langston, C. W., Cesnik, C. E. S., and Shin, S., "Vibratory Loads Reduction Testing of the NASA/Army/MIT Active Twist Rotor," *Journal of the American Helicopter Society*, Vol. 47, No. 2, 2002, pp. 123–133.

[16]Hodges, D. H., and Dowell, E. H., "Nonlinear Equation of Motion for the Elastic Bending and Torsion of Twisted Nonuniform Blades," NASA TND-7818, Dec. 1974.

[17]Coulliette, C., and Plotkin, A., "Aerofoil Ground Effect Revisited," *Aeronautical Journal*, Vol. 100, No. 992, 1996, pp. 65–74.